Applied Energy 267 (2020) 114987

Contents lists available at ScienceDirect

Applied Energy

journal homepage: www.elsevier.com/locate/apenergy

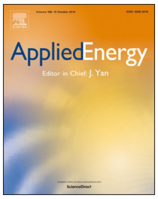

A scalable, causal, adaptive energy management strategy based on optimal control theory for a fuel cell hybrid railway vehicle☆

Hujun Peng[a,*], Jianxiang Li[a], Lars Löwenstein[b], Kay Hameyer[a]

[a] *Institute of Electrical Machines (IEM), RWTH Aachen University, Schinkel Straße 4, 52062 Aachen, Germany*
[b] *Siemens Mobility GmbH, Vienna, Austria*

HIGHLIGHTS

- The convexity of specific consumption curves is emphasized based on results of PMP.
- The dependency of co-states on SoC and the average fuel cell power is identified.
- A quantitative analytical formula is derived to determine the co-state.
- An excellent fuel economy results due to the accurate estimate of co-states.
- A scalable strategy due to its model-based characteristics.

ARTICLE INFO

Keywords:
Energy management
Fuel cell hybrid vehicles
Optimal control
Model-based control
Scalability

ABSTRACT

A scalable, causal, adaptive optimal control-based energy management strategy for the fuel cell hybrid train is designed. As learned from the results of offline Pontryagin's minimum principle (PMP)-based strategies, the convexity of the specific consumption curve is emphasized to improve the fuel economy. More important is that the dependency of the co-state on the state of charge (SoC) of batteries and the average fuel cell power is identified the first time. With the help of using the optimal control theory in a reverse way, a quantitative analytical formula is derived to determine the co-state based on the SoC and the average fuel cell power. The accuracy of the estimates, and the effectiveness of this strategy, under different weather, driving, and aging conditions, is validated by comparison to the results of offline PMP-based strategies. Thereby, a maximal deviation of the co-state average value compared to the offline results is 1.8%. An excellent fuel economy under a typical driving cycle of regional railway transports in Berlin, with only 0.03% more consumption for both summer and winter conditions, compared to the results of offline PMP, is resulted. Due to the model-based characteristics, the strategy can be scaled or transferred to other configuration systems or driving conditions without the loss of effectiveness.

1. Introduction

1.1. Background and motivations

About 50% of the railway network in Europe is operated by combustion engines [1]. In order to reduce greenhouse gas emissions, more electrification of the railway network is planned in the near future. However, it is not economically beneficial to electrify railway networks with low and medium use. Therefore, the hydrogen-powered railway vehicle is planned to replace the combustion engine-driven vehicles without high investment to electrify the entire railway network. Compared to the CO_2-based fuels, hydrogen is more economical and environmental friendly [2]. So far, the Proton Exchange Membrane (PEM) fuel cells have been attempted in the propulsion system for railway transportation. A 1200 kW hybrid locomotive powered with a 250 kW fuel cell as the prime energy source and lead-acid batteries as ancillary power was designed for possible commercial applications by the North American Consortium [3]. A 120 kW fuel cell-powered railcar is reported by Japan's Railway Technical Research Institute [4]. In China, Southwest Jiao-tong University introduced the first fuel cell-powered

---

☆ This work is funded by he German Federal Ministry for Economic Affairs and Energy (BMWi) under the National Innovation Program Hydrogen and Fuel Cell Technology (NIP) with the funding numbers of 03B10502B and 03B10502B2. The authors gratefully acknowledge the support by Siemens AG and NIP.

* Corresponding author.
E-mail address: hujun.peng@iem.rwth-aachen.de (H. Peng).

https://doi.org/10.1016/j.apenergy.2020.114987
Received 20 December 2019; Received in revised form 31 March 2020; Accepted 4 April 2020

locomotive in 2013 [5]. In Europe, Italy declared a road-switcher combined with a 120 kW fuel cell system and a 360 kWh lead-acid puffer battery system [6]. Notably, Alstom presented the world's first fuel cell-powered train named Coradia iLint powered by two 200 kW fuel cells and 110 kWh lithium-ion batteries in 2016, which started revenue service in Germany in 2018 [7]. Siemens is developing Mireo to replace the diesel engine-based train, and a fuel cell variant is also planned in cooperation with Ballard, which is expected to be operational in 2021 [8]. This is also the focus of this paper.

The fuel cell hybrid train of Mireo has no catenaries, and works under charge-sustaining conditions, which means, the fuel cell system provides the average load power along the entire driving cycle, while the battery system affords the transient high power during acceleration or absorbs negative load power during regenerative braking. Therefore, the degree of freedom to distribute load power between the fuel cell system and the battery system can be utilized to improve the performance of the driveline. Not only the fuel economy but also the operation of fuel cells and batteries with less stress is pursued in the design of energy management strategy [9].

1.2. Literature review

There are two types of energy management strategies: rule-based methods and optimization-based methods [10]. The rule-based methods are defined as a series of "if-then" rules to determine the control input, which are based on engineer expertise, intuition, safety considerations, and boundary constraints [11]. Their main advantage is the low computational burden and they are widely used in several commercial hybrid vehicles like the Toyota Mirai [12] and the Prius [13]. Furthermore, the rule-based methods can be classified into two types: deterministic rule-based methods und fuzzy rule-based methods. They are formulated in terms of fixed or fuzzy rules, which are influenced by various control parameters. Offline optimized control parameters can substantially advance the performance of rule-based strategies, as used in [14] to optimize the parameters of membership functions. However, these optimized parameters are strongly depending on the driving cycles and vehicle configurations, limiting the adaptivity of the rule-based methods in real-time applications.

The optimization-based methods are classified into global optimization methods and real-time optimization methods. The global optimization methods are implemented to calculate the global optimum solution for the entire driving cycles based on a priori information about future load situations. The most famous of them are dynamic programming and optimal control theory. Dynamic programming solves different optimization problems in discrete form based on Bellman's principles of optimality [15]. With the interpolation to evaluate the cost-to-go function of the new states, the algorithm is parallelized to improve computational efficiency [16]. Nevertheless, due to the remaining prohibitive computational load and the fact that the solutions are solely optimal for a given driving cycle, it is used as a reference strategy. In the stochastic dynamic programming (SDP), the Markov chain is used to describe the uncertain driving conditions, and the obtained solution by SDP is inferior to dynamic programming due to the insufficient information about the future driving situations [17]. For the optimal control-based strategy, the control law is based on the minimization of the so-called Hamiltonian function in each time instant under consideration of limits on controls. At lower computational effort, it outperformed an equivalent consumption minimization strategy (ECMS) regarding the fuel economy [18]. However, the estimation of the initial co-state has a non-trivial influence on the solution convergence if the driving cycle is not known.

For real-time optimization methods, the control variable is determined, minimizing a predefined cost function based on future equivalence assumption of the electric energy consumption. In general, the cost function should be mathematically formulated suitably for real-time applications in terms of memory resources and computational demands [13]. The most famous one is the above mentioned ECMS, which converts the electric energy consumption into an equivalent fuel consumption by using equivalent factors [19]. The crucial point is to estimate the equivalent factors considering different components' characteristics and dynamics of power sources. Because the estimation of the equivalent factors strongly influences the performance of ECMS, the research about ECMS can be differentiated in the two perspectives: searching the optimal static values or dynamic update of this equivalent factor [13]. The former can be realized using the evolutionary algorithm [20] regarding different driving cycles and vehicle configurations. The latter can be categorized into three subtypes: First, correcting the equivalent factor using PI-controller based on the offline reference trajectory [21]. Second, Introducing a penalty factor depending on the battery charging level to correct the equivalent factor [22]. Third, by using multi-dimensional look-up tables, which are offline calculated [23]. Another real-time optimization method is based on PMP. It is proved in [24] that ECMS is a simplified version of PMP-based strategy. As for the ECMS, the functionality of the PMP-based strategy is sensitive to the estimation of the co-state. Therefore, the dynamic correction of these values is implemented by using PI-control [25]. Compared to the rule-based strategies, the advantages of optimization-based energy control have been indicated in [26].

Furthermore, these real-time optimization methods can be combined with model predictive control (MPC) [27], in which the SoC reference value or an optimized SoC trajectory is pursued to be followed, as considered in the cost function. However, on one side, the fixed reference value limits the optimality of strategies, while the optimized SoC trajectory is strongly dependent on the optimality of the pattern predicting the optimal SoC trajectory. Moreover, in the case of ECMS or PMP-based MPC control, the estimation of the equivalent factor or co-state, which goes into the cost function, remains critical, as mentioned above.

Nowadays, it can be observed that the main trend of energy management is to acquire optimal solutions in real-time [28]. For this purpose, subsidiary adaptations tools such as pattern recognition, intelligent traffic systems, and prediction/estimation are integrated into optimization-based strategies [28]. However, the functionality of this subsidiary methods-based strategy is dependent on the offline training efforts, which does not guarantee the scalability and transferability of the strategy to other driving conditions and different aging components states.

In all, the PMP-based adaptive strategy is promising for real-time applications with the help of subsidiary tools if the available computational resources permit. However, the estimation of the co-state remains challenging, and the methods used, including driving pattern recognition, intelligent system, and prediction, to update the co-state do not show sufficient scalability, causality, and adaptivity regarding changes in terms of driving conditions, vehicle configurations, and components aging. The essential reason is that the dependency of the co-state on components characteristics and driving cycles is though identified. However, the quantitative formula to calculate the co-state is lacking. In other words, all the strategies about adaptive ECMS and PMP used in the reviewed literature utilize only the qualitative or partly quantitative relation of the co-state to the driving cycles.

1.3. Main work

In response to the above shortcomings, an analytical formula is derived for the first time to estimate the co-state for adaptive Pontryagin's minimum principle-based strategies (APMP). This formula is initiated by the discovery of dependency of the co-states on the average fuel cell power and SoC values from offline results. Thereby the co-state is determined by using the component characteristics. In the case of changes in vehicle configurations and components aging, the determination of the co-states or rather the whole strategy is adjusted, which ensures the scalability and adaptivity of the strategy. It is worth mentioning that the global fuel cell power is not known in advance in real-time. Therefore, a novel mechanism to estimate the average fuel cell power by using information from history and about the available terrain and time table is implemented to improve the estimate of the average fuel cell power.

1.4. Paper organization

The paper is organized as follows: in Section 2, the driveline modeling necessary for analyzing energy management is introduced. In Section 3, the offline PMP-based strategy and its results are described. Thereby, on the one side, the convexity of the specific consumption curve of the fuel cell system is emphasized to improve the fuel economy. On the other side, the dependency of the co-state on the average fuel cell power and SoC is identified. Subsequently, the analytical formula to determine the co-state, from the average fuel cell power and SoC, is derived. Then, the mechanism to estimate the average fuel cell power in the real-time application is introduced. In Section 4, the functionality of the APMP-based strategy under different driving cycles, weather, and aging conditions are approved based on simulations, compared to the results of offline PMP-based strategies. A thoughtful discussion based on that will be given. In Section 5, the conclusions and a possible outlook are given.

2. Driveline modeling

The configuration of the parallel hybrid train powered by fuel cells and batteries is displayed in Fig. 1. In order to study the influence of energy management strategies on the fuel economy, it is common to stationary model the most components of the driveline except the train velocity and SoC, without dynamic in other components considered. Due to symmetry, power flow is modeled for a half train instead of a whole train, as shown in Fig. 2. The modeling of components will be explained in the following sections.

2.1. Environment model

In the environment model, driving cycles and slope profiles of three routes in Germany are defined, as presented in Fig. 3. The driving cycle 1 of a distance of 145.8 km and travel time of 8110 s belongs to the regional train 1 between Aachen and Cologne, and it goes downhill and then uphill. The driving cycle 2 of a distance of 154 km and 8192 s corresponds to the Mannheim-Karlsruhe-Basel railway in the State of Baden-Wüttemberg, and it goes uphill and then downhill. The driving cycle 3 of a distance of 584.5 km and 68213 s belongs to the regional train 27, which travels through Berlin and Brandenburg. The driving cycle 3 has a much smaller slope than the former two. Information about route parameters, including terrain gradient, velocity limits, traveling time between stations, and hold time in each station, comes from project partners. These driving cycles are determined by using dynamic programming with the minimization of hydrogen consumption as the goal [29], with algorithm parallelized as [16]. The number of passengers is assumed to be 120, each with a mass of 75 kg.

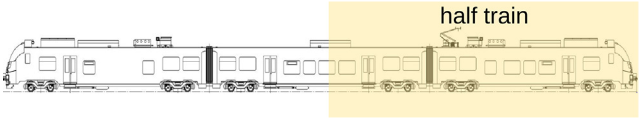

Fig. 2. A half train.

2.2. Longitudinal dynamic

The various forces acting on the vehicle are illustrated in Fig. 4. The forces acting on the train can be broadly classified as the traction force F_{trac} acting on the wheels of the train and the other various resistant forces. The various resisting forces on the vehicle body include aerodynamic drag F_{aero}, uphill resistance F_{grade}, acceleration force F_a, and rolling resistance F_{roll}, as shown in (1). During mechanical braking, there is also resistance force represented by F_b. The positive direction of the resistance forces is defined against the train velocity v.

$$F_a = F_{\text{trac}} - F_{\text{roll}} - F_{\text{aero}} - F_{\text{grade}} - F_b, \tag{1}$$

which can be expanded as follows:

$$m\cdot\frac{dv}{dt} = F_{\text{trac}} - \mu_r mg\cos(\phi) - 0.5\rho_{\text{air}} C_d A_f v^2 - mg\sin(\phi) - F_b, \tag{2}$$

where m is the train mass, μ_r the coefficient of the rolling resistance; C_d the aerodynamic coefficient, ρ_{air} the air density, A_f the front area, g the gravitational acceleration, and ϕ the angle of slope. The above mentioned parameters can be found in Table 1.

2.3. Electrical machines

Three high-speed induction machines of 220 kW rating power are used to drive a half train, to ensure a maximal speed of 160 kmh and an acceleration capability of 1.2 m/s^2. The electrical machines are stationary modeled by using lookup tables without considering the machine mechanical dynamic due to the short time constant compared to the train dynamic. Those lookup tables come from post-processing of results of Finite Element Analysis, and they have torque demand and the rotational speed as inputs. A total of four lookup tables, as displayed in Fig. 5, are needed to model the loss along the driveline. Besides the power loss, the other three lookup tables are required to calculate the inverter loss. The current directly influences the inverter loss, and the power factor determines the current sharing between IGBT and diode. The motor voltage influences the modulation degree, which can also influence the inverter loss. The ratio of the gear is assumed to be 10, and its efficiency 0.98. The vehicle wheel radius is 0.425 m. With the help of these parameters, the machine torque is converted to the traction force on the tire. All related parameters can be found in Table 2.

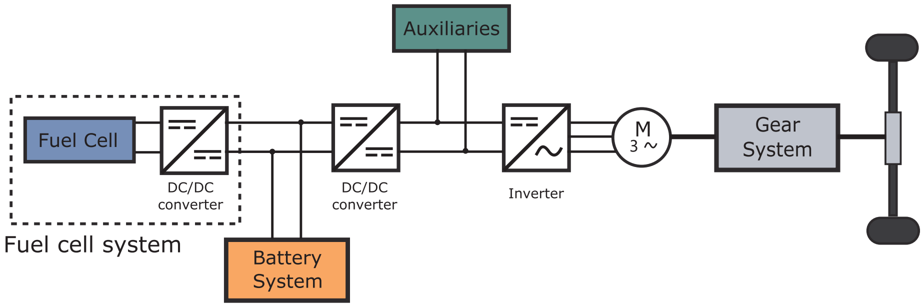

Fig. 1. System configuration of hybrid train.

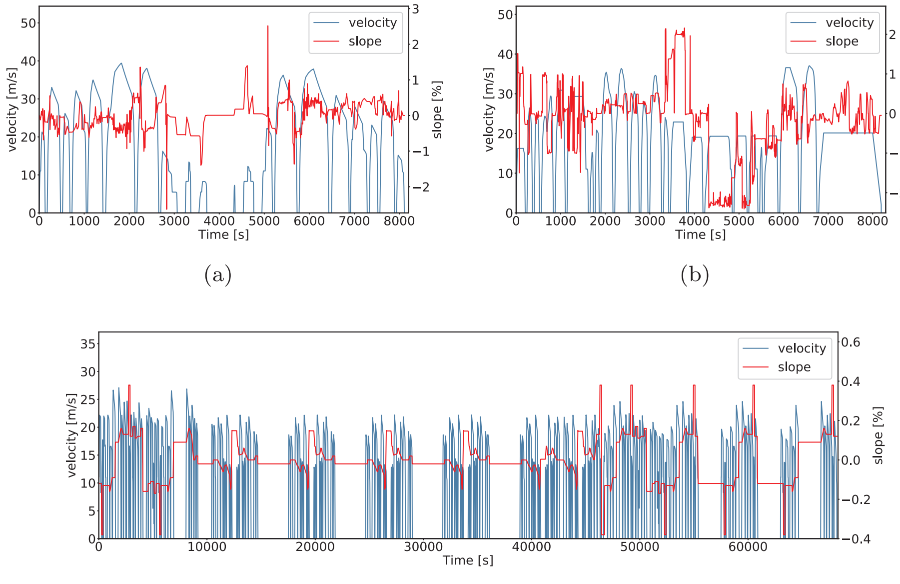

(a)

(b)

(c)

Fig. 3. Driving cycles: (a) driving cycle 1 with distance of 145.8 km and travel time of 8110 s, (b) driving cycle 2 with a distance of 154 km and travel time of 8192 s, (c) driving cycle 3 with a distance 584.5 km and travel time of 68213 s.

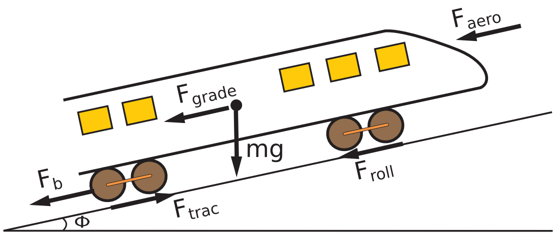

Fig. 4. Forces acting on the train.

Table 1
Parameters related to longitudinal dynamic.

parameters	symbols	values	units
train mass (with passengers included)	m	60000	kg
gravitational acceleration	g	9.81	m/s^2
rolling resistance coefficient	μ_r	0.0015	–
air density	ρ_{air}	1.4	kg/m^3
aerodynamic coefficient	C_d	0.15	–
front area	A_f	10	m^2

2.4. DC/AC inverter

The inverter loss depends on the machine current, machine voltage, power factor, switching frequency or machine speed, DC-link voltage, and semiconductor temperature. Nevertheless, temperature and DC-link voltage are in practice controlled to be constant. In the simulation, the DC-link voltage is 1200 V, and the temperature is assumed to be 120°C. Therefore, the inverter is modeled using four-dimensional lookup tables, with the machine voltage, machine current, machine speed, power factor as inputs, shown in Figs. 6 and 7. The influence of the power factor and motor speed on loss is also displayed, based on a working point with phase voltage and current equal to 350 V and 200 A. The lookup tables are derived by using simulation with the help of software Plecs, and the simulated model is presented in Fig. 8. Three alternate current sources with a phase shift of 120 degrees to each other are applied as the symmetrical load. Through modulation control, the amplitude of phase voltage and the power factor can be adjusted. Besides that, the switching frequency is adjusted proportionally to the motor speed to reduce the switching loss of the converter at low motor speed. The switching frequency is ten times the ground frequency of the current supply f_1. The semiconductor module has a rated current of 450 A and a breakdown voltage of 3300 V, whose datasheet belongs to the product of Infineon named FF450R33T3E3. Other parameters of inverters can be found in Table 3.

2.5. Auxiliary consumption

The auxiliary systems correspond to the non-driving function of the hybrid trains, which include heating, compressors, ventilation systems, and air conditioning. In order to determine the energy consumption of an air conditioning system, the thermal power introduced into the passenger compartment has to be considered, including heat conduction, convection and radiation, passenger heat generation, ventilation and the heat from electrical components [30]. Since the focus lies on hybrid strategies in this work, a static thermal model is used to simplify the calculation of energy consumption. It is assumed -5 °C in winter, 35 °C in summer, and 21 °C in the cabin. In the simulation, the power, including the onboard electrical consumers, is estimated to be 83 kW in winter and 55 kW in summer, respectively.

2.6. DC/DC converter

For the DC/DC converter, the coupling between thermal and electrical modeling is considered. A thermal network, as shown in Fig. 12, is used to calculate the temperature of semiconductors, and the heatsink temperature is set to be 40 °C. In order to consider the nonlinearity, simulation with the help of the software Plecs is used to determine the lookup tables, whose model with three parallel branches is presented in Fig. 9. The converter loss is dependent on the load current, DC-link voltage, battery voltage, and semiconductor temperature. The power loss lookup tables are displayed in Figs. 10 and 11 regarding different temperatures and battery voltages. The effect of the temperature and battery voltage on the loss can be identified, based on an operational point with the DC-link voltage and load current equal to 1200 V and 350 A. The semiconductor module is the same as that in the DC/AC converter. Other parameters related to the loss can be found in Table 4.

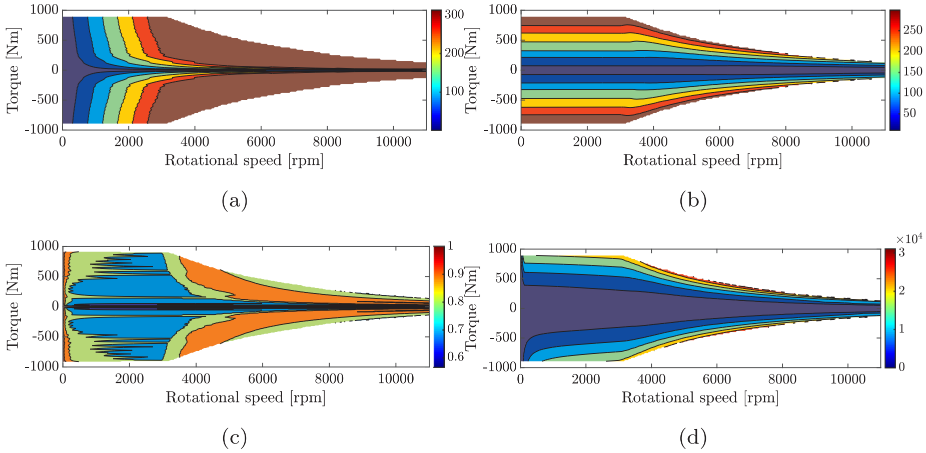

Fig. 5. Electrical machines characteristics: (a) Electrical machine voltage in V, (b) Electrical machine current in A, (c) Electrical machine power factor, (d) Electrical machine loss in W.

Table 2
Parameters related to electrical machines.

parameters	values	units
number of poles	4	–
rated power (kW)	220	kW
maximal power (kW)	300	kW
rated rotational speed	3200	rpm
maximal rotational speed	12000	rpm
gear ratio	10	–
gear efficiency	0.98	–
number of motors	3	–
wheel radius	0.425	m

2.7. Fuel cell system

The efficiency of the fuel cell system is strongly dependent on the dynamic conditions, and especially related to the operative conditions of auxiliary sub-systems including stacking cooling, reactant feeding, and humidification [30]. As the focus of this paper lies in the design of energy management strategy to improve fuel economy, it is general to model the fuel cell system stationary, and a model based on a specific consumption curve of the fuel cell system in Fig. 13 is used. The convexity of the curve can be identified, as described in (3).

$$\dot{m}_{\mathrm{H_2}}(\alpha\cdot P_{\mathrm{fc},1} + (1-\alpha)\cdot P_{\mathrm{fc},2}) < \alpha\cdot\dot{m}_{\mathrm{H_2}}(P_{\mathrm{fc},1}) + (1-\alpha)\cdot\dot{m}_{\mathrm{H_2}}(P_{\mathrm{fc},2}), \tag{3}$$

where $\dot{m}_{\mathrm{H_2}}$ represents the mass flow depending on the net fuel cell power. The convexity will be utilized to derive an analytical formula to determine the co-state later. Correspondingly, its efficiency curve is displayed in Fig. 14. It is worth mentioning that the product of Ballard HD7 is used as the fuel cell system and its detailed parameters about its inner construction are not available.

2.8. Battery system

The battery model of the lithium-ion high-performance cell used is parameterized by using real measurement data consisting of pulse tests and electrochemical impedance spectroscopy. The cells are interconnected to modules, which are connected to a battery pack with nominal voltage of 850 V and energy capacity of 200 kWh. Here an equivalent circuit model with 3 R-C branches is used for the entire battery system, as shown in Fig. 15. The dependency of various parameters on the SoC and temperature can be found in Fig. 16. The heat loss is dissipated by active liquid cooling. With the active cooling, the temperature of the battery pack is controlled to be 25 °C, and the thermal modeling is not considered. The characteristic curves of the open-circuit voltage and R_0 at 25 °C are displayed in Fig. 17, which shows an obvious dependency on SoC.

3. Adaptive optimal control-based strategy

In this section, the scalable, causal, and adaptive optimal control-based strategy will be detailedly displayed. In the first step, the offline PMP-based energy management strategy is briefly introduced, and the sensitivity of the strategy on the estimate of co-states is emphasized. With the help of offline PMP, on the one side, the convexity of the specific consumption curve of the fuel cell system is identified to improve the fuel economy. On the other side, the dependency of the co-state on SoC and the average fuel cell power is the first time identified. This new discovery initiates the possibility of determining the co-state analytically. With the help of reversely using the optimal control theory, the formula to determine the co-state is derived. Furthermore, to eliminate the sensitivity of the strategy depending on the estimates of the co-state, the average fuel cell power is over again estimated.

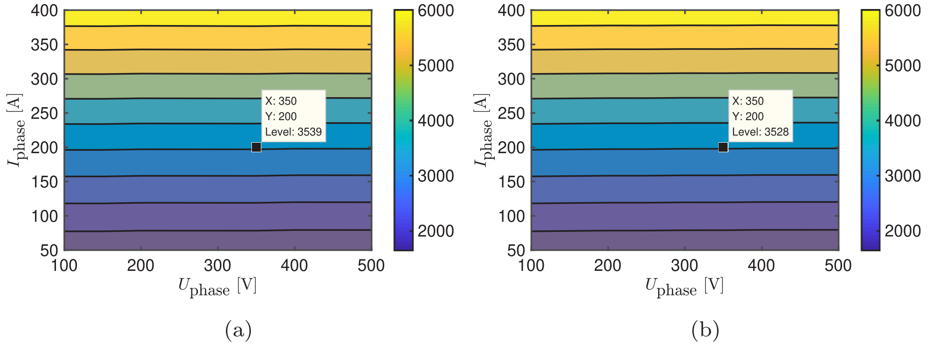

Fig. 6. Inverter loss in W at low motor speed $n_{\mathrm{motor}} = 3000$ rpm: (a) under $\cos\phi = 0.8$, (b) under $\cos\phi = 0.7$.

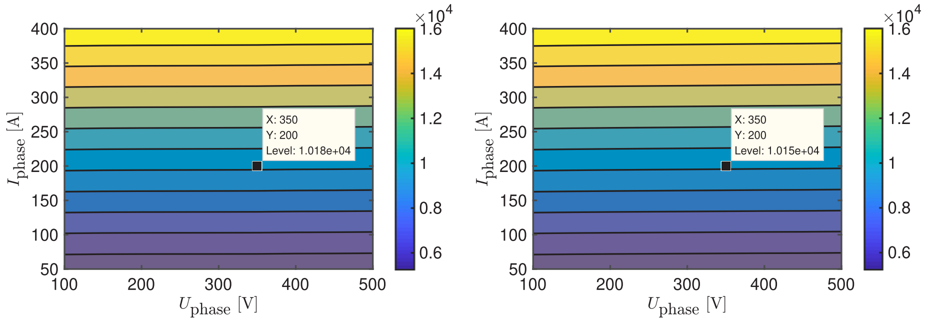

(a)

(b)

Fig. 7. Inverter loss in W at low motor speed n_{motor} = 10000 rpm: (a) under cosϕ = 0.8, (b) under cosϕ = 0.7.

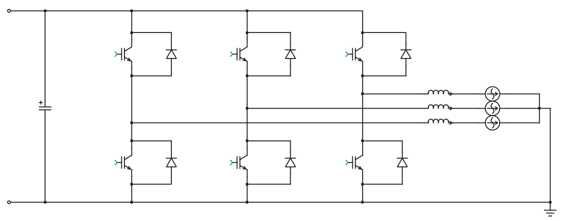

Fig. 8. Simulated model of DC/AC inverter in Plecs.

Table 3
Parameters related to DC/AC inverter.

parameters	values	units
number of inverter	3	–
DC-link voltage	1200	V
module temperature	120	°C
switching frequency	$10\cdot f_1$	Hz
breakdown voltage of the semiconductor module	3300	V
rated current of the semiconductor module	450	A

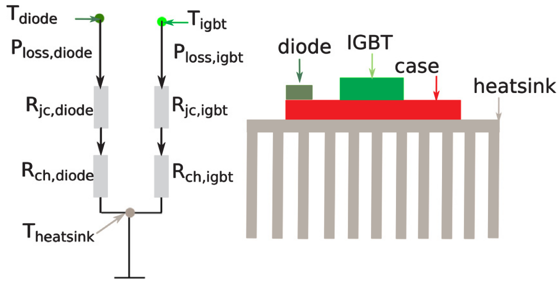

Fig. 12. Thermal network of DC/DC converter.

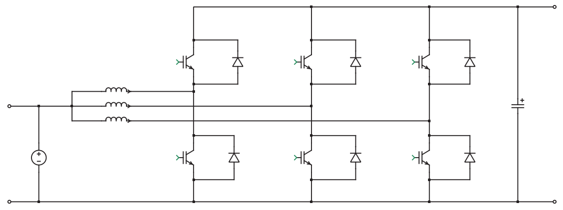

Fig. 9. Simulated model of DC/DC converter in Plecs.

3.1. Basics of offline PMP

For using the optimal control to get the optimal offline strategy, the formulation of the Hamiltonian function plays a central role, which is formulated as follows:

$$H(SoC, P_{fc}, \lambda, t) = \dot{m}_{H_2}(P_{fc}) + \lambda(t)\cdot S\dot{o}C(t) \tag{4}$$

where the $\dot{m}_{H_2}$ is the mass flow with the unit of g/s, which depends on the fuel cell power P_{fc}, as shown in Fig. 13, $SoC(t)$ the state variable, and the $\lambda(t)$ the co-state with the unit of g. The dynamics of the state and the co-state are defined according to the optimal control theory as follows:

$$S\dot{o}C(t) = -\frac{I_{bat}}{Q_{bat}}, \tag{5}$$

for the state dynamic, and

$$\dot{\lambda}(t) = -\frac{\partial H(SoC, P_{fc}, \lambda, t)}{\partial SoC}, \tag{6}$$

for the co-state dynamic. With the substitution of the Hamiltonian function defined in (4) into (6), the co-state dynamic can be expanded as

$$\dot{\lambda}(t) = -\frac{\partial \dot{m}_{H_2}}{\partial SoC} - \lambda(t)\cdot\frac{\partial S\dot{o}C}{\partial SoC} = 0 - \lambda(t)\cdot\frac{\partial S\dot{o}C}{\partial SoC}, \tag{7}$$

whereby the derivative of the mass flow with respect to SoC equals zero, because the mass flow is independent on SoC.

The battery current I is related to the load power and the fuel cell power as follows:

$$I\cdot(V_{oc,bat} - R_{0,bat}\cdot I) = P_{bat} = P_{load} - P_{fc}. \tag{8}$$

From that, the battery current can be written in function of the load power and the fuel cell power:

$$I = \frac{V_{oc,bat} - \sqrt{V_{oc,bat}^2 - 4\cdot(P_{load} - P_{fc})\cdot R_{0,bat}}}{2\cdot R_{0,bat}}, \tag{9}$$

which can be substituted into (5):

$$S\dot{o}C(t) = -\frac{V_{oc,bat} - \sqrt{V_{oc,bat}^2 - 4\cdot(P_{load} - P_{fc})\cdot R_{0,bat}}}{2\cdot Q_{bat}\cdot R_{0,bat}}. \tag{10}$$

It is obvious that the change rate of SoC is not directly related to SoC, however, the open-circuit voltage $V_{oc,bat}$ and the resistance $R_{0,bat}$ are dependent on SoC, as displayed in Fig. 17. Then, the derivative of the change rate of SoC with respect to SoC can be reformulated as follows:

$$\frac{\partial S\dot{o}C}{\partial SoC} = \left(\frac{\partial S\dot{o}C}{\partial V_{oc,bat}}\cdot\frac{\partial V_{oc,bat}}{\partial SoC} + \frac{\partial S\dot{o}C}{\partial R_{0,bat}}\cdot\frac{\partial R_{0,bat}}{\partial SoC}\right), \tag{11}$$

which can be substituted into (7) to calculate the co-state dynamic:

$$\dot{\lambda}(t) = -\lambda\left(\frac{\partial S\dot{o}C}{\partial V_{oc,bat}}\cdot\frac{\partial V_{oc,bat}}{\partial SoC} + \frac{\partial S\dot{o}C}{\partial R_{0,bat}}\cdot\frac{\partial R_{0,bat}}{\partial SoC}\right). \tag{12}$$

With utilization of (10) follows the partial derivative of the change rate of SoC with respect to the open-circuit voltage

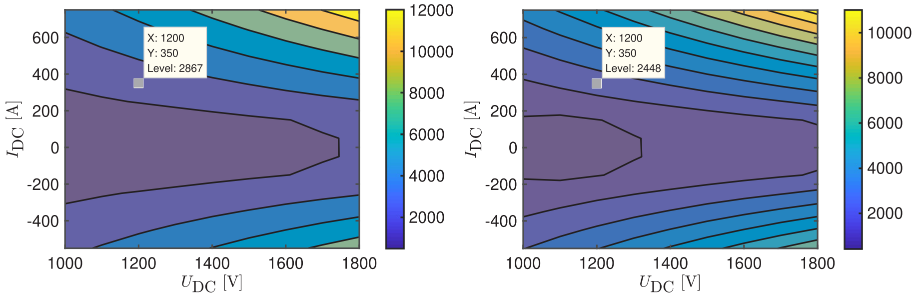

(a) (b)

Fig. 10. DC/DC converter loss in W depending on voltage and load current at DC-link with battery voltage equal to 850 V: (a) under 150 °C, (b) under 80 °C.

$$\frac{\partial \dot{SoC}}{\partial V_{\mathrm{oc,bat}}} = -\frac{1}{2\cdot Q_{\mathrm{bat}} R_{0,\mathrm{bat}}}\cdot\left(1-\frac{V_{\mathrm{oc,bat}}}{\sqrt{V_{\mathrm{oc,bat}}^2-4\cdot(P_{\mathrm{load}}-P_{\mathrm{fc}})R_{0,\mathrm{bat}}}}\right), \tag{13}$$

and the partial derivative of the change rate of SoC with respect to the inner resistance $R_{0,\mathrm{bat}}$

$$\frac{\partial \dot{SoC}}{\partial R_{0,\mathrm{bat}}} = \frac{1}{2\cdot Q_{\mathrm{bat}} R_{0,\mathrm{bat}}^2}\left(\frac{2\cdot(P_{\mathrm{load}}-P_{\mathrm{fc}})R_{0,\mathrm{bat}}-V_{\mathrm{oc,bat}}^2}{\sqrt{V_{\mathrm{oc,bat}}^2-4\cdot(P_{\mathrm{load}}-P_{\mathrm{fc}})R_{0,\mathrm{bat}}}}+V_{\mathrm{oc,bat}}\right). \tag{14}$$

The derivatives of the open-circuit voltage and the inner resistance with respect to SoC, which are also in function of SoC, can be derived from the characteristic curves shown in Fig. 17, and the results are shown in Fig. 18.

According to PMP, the control is determined to minimize the Hamiltonian function in each instant as follows:

$$P_{\mathrm{fc}}^*(t) = \underset{P_{\mathrm{fc}}(t)}{\mathrm{argmin}}\, H(SoC,\, P_{\mathrm{fc}},\, \lambda,\, t). \tag{15}$$

Table 4
Parameters related to DC/DC converter.

parameters	values	units
switching frequency	1000	Hz
number of parallel branches	3	–
resistance of inductor pro branch	0.15	mΩ
inductance pro branch	1.3	mL
capacitor	6	mF
breakdown voltage of the semiconductor module	3300	V
rated current of the semiconductor module	450	A
$R_{\mathrm{ch,igbt}}$, case to heatsink, per IGBT	17.4	K/kW
$R_{\mathrm{jc,igbt}}$, junction to case, per IGBT	28.4	K/kW
$R_{\mathrm{ch,diode}}$, case to heatsink, per diode	19.3	K/kW
$R_{\mathrm{jc,diode}}$, junction to case, per diode	45.5	K/kW
T_{heatsink}, Temperature of heatsink	40	°C

If the initial values of the state and the co-state are known, they can be updated in each instant with the help the dynamic Eqs. (10) and (12). However, in the physical world, only the initial and end values of the states are known, from which the name of two-point boundary value problems come. Due to the nonlinearity of the system defined by the dynamic Eqs. (10) and (12), there are only numeric solutions in this case. For that purpose, the shooting method by using a bidirectional search is utilized to find the right initial co-state. For the boundary conditions, the initial and end SoC are chosen to be 0.5. Due to the widely known PMP, only some essential results are displayed in Fig. (19). Thereby, Fig. 19a displays the end SoC value depending on the initial co-state values, and a monotonic relation between them can be identified. The end SoC value is sensitive to the initial co-state in the neighborhood of the true value of the co-state, which means a small error in estimates of the co-state value leads to enormous different solutions. Fig. 19b depicts SoC trajectories corresponding to different initial co-states, which also reflects the sensitivity of the solutions against the initial values of the co-state. Therefore, the core of using PMP in energy management for hybrid vehicles is to estimate the co-state accurately in real-time.

3.2. Results of offline PMP

The shooting methods are used to find the right initial co-state values for different driving cycles under different weather. The results regarding the fuel cell power trajectories, SoC trajectories, and the co-state trajectories for different driving cycles are displayed in (Fig. 20), (Fig. 21) and (Fig. 22), respectively. Recognized from the SoC trajectories in Figs. 20c, 21c and 22c, the condition of charge-sustaining is fully satisfied, which means the estimates of the initial co-states for all cases are correct. Besides that, the SoC trajectories are fast identical under summer and winter because, under offline PMP, the fuel cell system covers the average load power for both seasons, and the battery current due to acceleration and regenerative braking is fast identical. From the co-state trajectories in Figs. 20b, 21b and 22b, a changeable co-state can be observed. Therefore, strategies, as found in much literature, with an assumed constant value of the co-state, can not optimize power distribution. More interesting is that the average amplitude

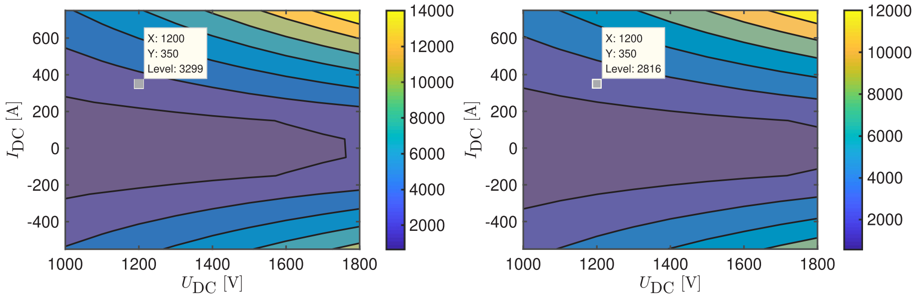

(a) (b)

Fig. 11. DC/DC converter loss in W depending on voltage and load current at DC-link with battery voltage equal to 740 V: (a) under 150 °C, (b) under 80 °C.

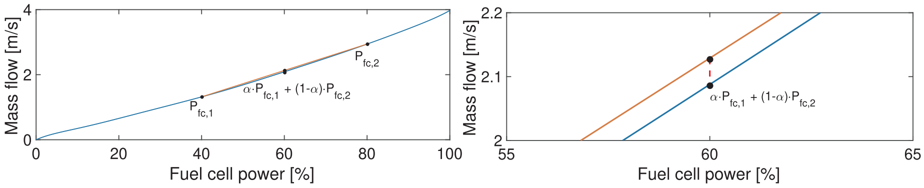

(a) (b)

Fig. 13. Specific consumption curves of the fuel cell system: (a) Without zoom, (b) Zoom in.

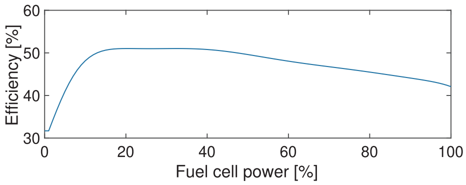

Fig. 14. Efficiency curve of the fuel cell system.

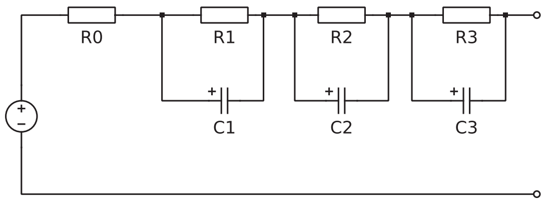

Fig. 15. Equivalent circuit with 3 R-C branches for the battery system.

of the co-state in summer is more than that in winter for all three driving cycles, which is related to the different average load power in different seasons. The dependency of the amplitude of the co-state on the average fuel cell power can be identified in Table 5. The average amplitude of the co-state decreases as the average fuel cell power decreases. The analytical relations between the co-state values and the average fuel cell power will be derived in the next subsection. More notable is that the fuel cell power for different driving cycles under different weather, as shown in Figs. 20a, 21a and 22a, stays near its average values, along with small and frequent dynamics. It can be derived that the power distribution with the fuel cell power approximately close to its average values results in an excellent fuel economy. The reason for that lies in the convexity of the specific consumption of the fuel cell system. To meet the charge-sustaining condition, the total electrical energy from the fuel cell system should be equal to the sum of the total load energy and the total battery loss energy as:

$$\int_0^T P_{\mathrm{fc}}(\tau)d\tau = \int_0^T (P_{\mathrm{load}}(\tau) + P_{\mathrm{loss,bat}}(\tau))d\tau, \tag{16}$$

where T is the travel time. The average fuel cell power is defined as follows:

$$\overline{P}_{\mathrm{fc}} = \frac{\int_0^T P_{\mathrm{fc}}(\tau)d\tau}{T}. \tag{17}$$

Then, the convexity, as described in (3), can be extended for the average fuel cell power along with the entire driving cycles:

$$\dot{m}_{\mathrm{H_2}}(\overline{P}_{\mathrm{fc}}) < \frac{\int_0^T \dot{m}_{\mathrm{H_2}}(P_{\mathrm{fc}}(\tau))d\tau}{T}. \tag{18}$$

Therefore, a concentration of working points near an average value results in an excellent fuel economy than a distribution of working points, which is consistent with the results of offline PMP. Then, the average value, close to which the fuel cell system works, should be equal to the sum of the average load and the average battery loss, due to the charge-sustaining, as follows:

$$\overline{P}_{\mathrm{fc}}^{*} = \overline{P}_{\mathrm{load}} + \overline{P}_{\mathrm{loss,bat}}, \tag{19}$$

as derived with the help of division of both sides in (16) by the travel time T.

Other relevant parameters related to the offline results are summarized in Table (5), including the average load power, the average battery loss, the average fuel cell power, and the average amplitude of the co-state. Thereby, the hydrogen consumption is scaled back for a whole train instead of a half train.

3.3. Dependency of the co-state on SoC and the average fuel cell power

Besides displaying its trajectories in the time domain in the last subsection, the co-state is here plotted in the function of SoC for different driving cycles under different weather, respectively, as shown in (Fig. 23). The amplitude of co-state under the optimal control increases with SoC increased, which is entirely contrary to the co-state correction mechanism adopted in all reviewed literature about ECMS and PMP, which decreases the amplitude of the co-state as SoC goes up. The reason for this lies in the higher open-circuit voltage of batteries at higher SoC, as shown in Fig. 17. According to the energy-conservation principle, for the same incremental increase of SoC at a higher SoC level, more electrical energy is required, which also means more hydrogen consumed to charge the battery system. Besides that, with the average fuel cell power in winter increasing compared to that in summer, the average amplitude of the co-state increases, as mentioned in the last subsection. The reason is that in winter, the fuel cell system works at higher average power, whose corresponding efficiency is also lower than that in summer, as shown in (Fig. 14). That means, for the same incremental increase of SoC, more hydrogen consumption is required, and the amplitude of the co-state goes up. More notably, the value of co-states under optimal control shows a significant concentration under different combinations of SoC and the average fuel cell power. It can be inferred that the co-state can be simplified to be a single-valued function of SoC and the average power. This function can be approximated by using data from offline PMP for various driving conditions and weather conditions, and the approximated curves are also shown in corresponding figures.

3.4. Analytical formula to derive the co-state

According to the optimal control theory, the control is determined to minimize the Hamiltonian function, as defined in (15). It is reasonable to assume, that the partial differential of the Hamiltonian with respect to the control for the optimal control is zero, as follows:

$$\left.\frac{\partial H}{\partial P_{\mathrm{fc}}}\right|_{P_{\mathrm{fc}}=P_{\mathrm{fc}}^{*}} = \frac{\partial \dot{m}_{\mathrm{H_2}}}{\partial P_{\mathrm{fc}}} + \lambda \left.\frac{\partial S\dot{o}C}{\partial P_{\mathrm{fc}}}\right|_{P_{\mathrm{fc}}=P_{\mathrm{fc}}^{*}} = 0, \tag{20}$$

where P_{fc}^{*} represents the actual optimal control. As learned from the last subsection, the fuel cell power under the optimal control is close to its average value, and then the average value is substituted into (20) as follows:

$$\left.\frac{\partial H}{\partial P_{\mathrm{fc}}}\right|_{P_{\mathrm{fc}}=\overline{P}_{\mathrm{fc}}} = \frac{\partial \dot{m}_{\mathrm{H_2}}}{\partial P_{\mathrm{fc}}} + \lambda \left.\frac{\partial S\dot{o}C}{\partial P_{\mathrm{fc}}}\right|_{P_{\mathrm{fc}}=\overline{P}_{\mathrm{fc}}} = 0, \tag{21}$$

whereby the partial derivative of the change rate of SoC with respect to the fuel cell power can derived from (10):

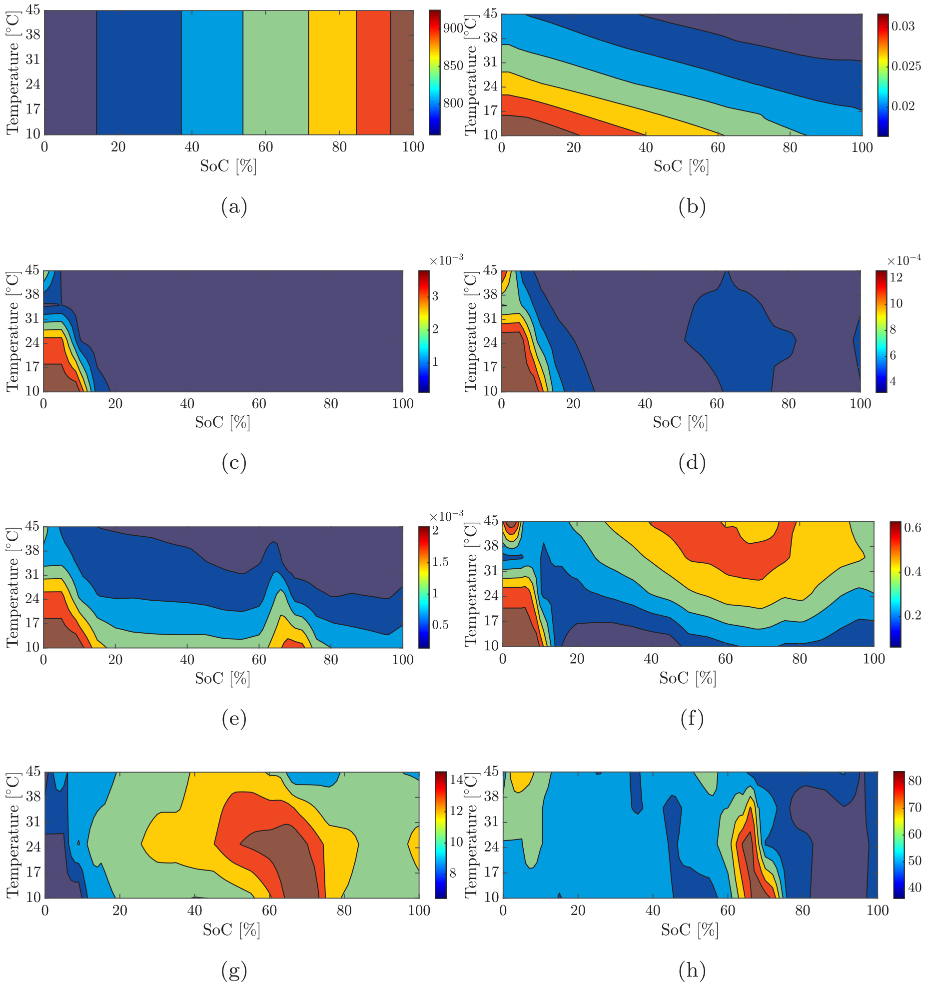

(a) (b) (c) (d) (e) (f) (g) (h)

Fig. 16. Parameters of the equivalent circuit components of the battery system: (a) Open-circuit voltage in V, (b) R_0 in Ω (c) R_1 in Ω, (d) R_2 in Ω, (e) R_3 in Ω, (f) Time constant due to $R_1 \cdot C_1$ in seconds, (g) Time constant due to $R_2 \cdot C_2$ in seconds, (h) Time constant due to $R_3 \cdot C_3$ in seconds.

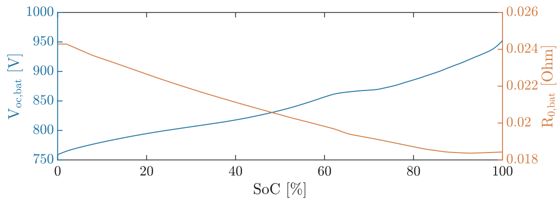

Fig. 17. Open-circuit voltage and R_0 of the whole battery system depending on SoC at 25 °C.

$$\frac{\partial \dot{SoC}}{\partial P_{fc}} = \frac{1}{Q_{bat}} \cdot \frac{1}{\sqrt{V_{oc,bat}^2 - 4\cdot(P_{load} - P_{fc})R_{0,bat}}}. \tag{22}$$

After its substitution into (21) follows the analytical formula to determine the co-state:

$$\lambda = -\frac{\partial \dot{m}_{H_2}}{\partial P_{fc}} \cdot \left(Q_{bat} \cdot \sqrt{V_{oc,bat}^2 - 4\cdot(P_{load} - P_{fc})R_{0,bat}}\right)\Bigg|_{P_{fc}=\overline{P}_{fc}}, \tag{23}$$

whereby the derive of the mass flow with respect to the fuel cell power can be derived from the specific consumption curve, which is also a function of fuel cell power, as depicted in Fig. 24. The open-circuit voltage and the inner resistance are dependent on SoC, as shown in Fig. 17. However, an assumption have to be made for the value of the load power. A reasonable but straightforward assumption is that the load power equals the average fuel cell power because, in this case, the battery loss equals to zero. Then the analytical formula to determine the co-state can be simplified to

$$\lambda = -\frac{\partial \dot{m}_{H_2}}{\partial P_{fc}} \cdot Q_{bat} \cdot V_{oc,bat}\Bigg|_{P_{fc}=\overline{P}_{fc}}, \tag{24}$$

then it is evident that the co-state is a function of SoC included in the open-circuit voltage, and the average fuel cell power included in the

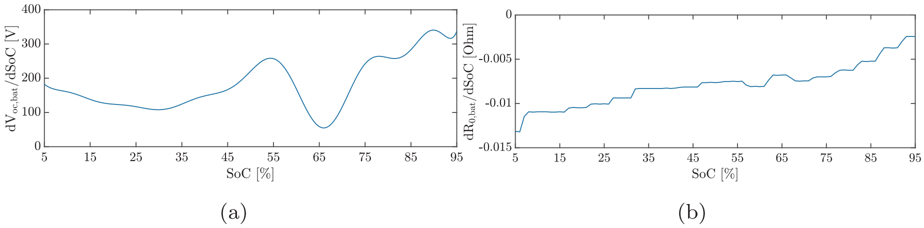

(a) (b)

Fig. 18. Derivatives of the open-circuit voltage $V_{oc,bat}$ and the inner resistance $R_{0,bat}$ with respec to SoC in function of SoC: (a) $\frac{\partial V_{oc,bat}}{\partial SoC}$, (b) $\frac{\partial R_{0,bat}}{\partial SoC}$.

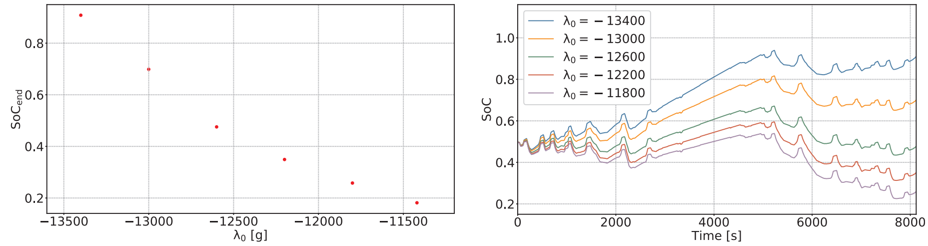

(a) (b)

Fig. 19. Results of Shooting methods: (a) End value of SoC dependent on the initial co-state value, (b) SoC trajectories under different initial co-state values.

derivative of the mass flow with respect to the fuel cell power.

According to the equation, the co-state can be plotted as the function of SoC and the average fuel power with its value as the same as the offline case, as shown in Fig. 25. After comparison to the fitted curve from the offline results, the effectiveness of the analytical formula is validated. It is worth mentioning that the parameters required in the analytical formula are the fuel cell system and battery system characteristics, which depend only on the components and system configuration instead of specific driving cycles or driving patterns. Therefore, this analytical formulation to estimate the co-state can be scaled or transferred to other system configuration without the loss of effectiveness. Even in the case of component degradation, the formula adapts itself to maintain accuracy regarding the actual component characteristics.

This analytical formula can be utilized to correct the co-state regularly, in order to eliminate the sensitivity of the strategy on the values of the co-state, as mentioned before, which is the most challenging task faced with ECMS. During the remaining time, the co-state evolves as the dynamic Eq. (12) shows, to utilize the local optimality based on PMP.

However, the required average fuel cell power along the whole drive cycle is unknown in the real-time application. Therefore, the history information of the load and battery loss power is utilized to estimate the global average values. The remaining task is to determine when to correct the co-state and how to estimate the average fuel cell power from history information correctly.

3.5. Mechanism of updating the average fuel cell power

Typically, vast load power is demanded during acceleration, and negative power is regenerated during regenerative braking operation. Therefore, the average load power is overestimated during acceleration of the vehicle and underestimated during regenerative braking, when compared to the global average load power. To solve this problem, the time instant, when the train leaves each station along the driving cycle, is chosen to correct the co-state, as shown in Fig. 26. This instant also applies to estimate the average battery loss well due to the same reason. In this way, the average fuel cell power is estimated to be

$$\overline{P}_{\mathrm{fc}}(t)=\frac{\int_0^t P_{\mathrm{load}}(\tau)+P_{\mathrm{loss,bat}}(\tau)d\tau}{t}, \tag{25}$$

whereby the load power is the sum of various loss power:

$$P_{\mathrm{load}}(t)=F_{\mathrm{trac}}\cdot v+P_{\mathrm{loss,driveline}}+P_{\mathrm{aux}} \tag{26}$$

with help of the longitudinal dynamic equation in (1), the above equation can be expanded to

$$P_{\mathrm{load}}(t)=\left(m\cdot\frac{dv}{dt}+F_{\mathrm{roll}}+F_{\mathrm{aero}}+F_{\mathrm{grade}}+F_{\mathrm{b}}\right)\cdot v+P_{\mathrm{loss,driveline}}+P_{\mathrm{aux}}, \tag{27}$$

where P_{aux} represents the auxiliary consumption, $P_{\mathrm{loss,driveline}}$ the sum of power loss in the DC/DC converter, gear, motor, inverter, and the remaining power is required to overcome the different resistances along

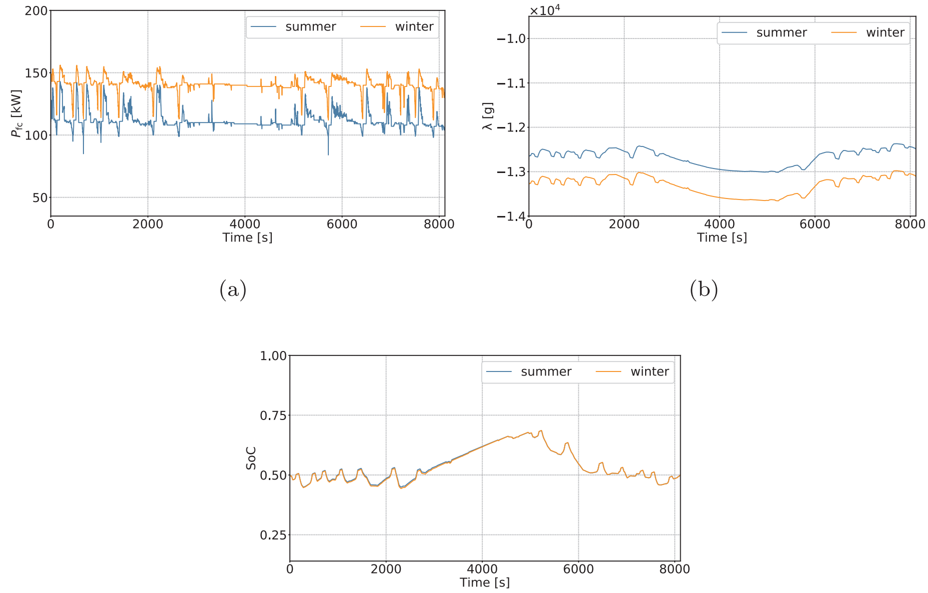

(a) (b)

(c)

Fig. 20. Results of PMP for the driving cycle 1: (a) Fuel cell power trajectories, (b) Co-state trajectories, (c) State trajectories.

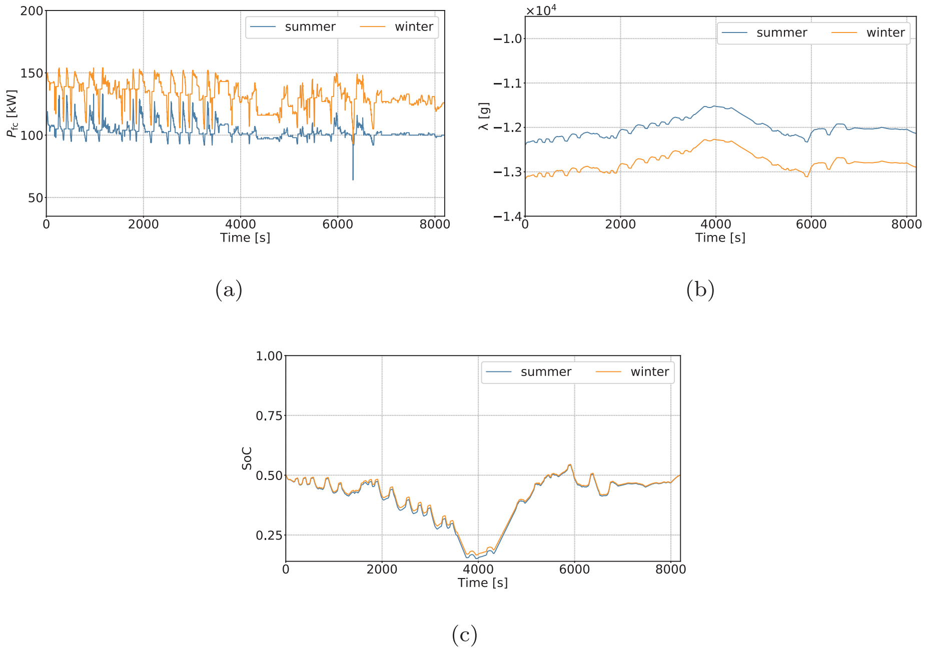

(a) (b)

(c)

Fig. 21. Results of PMP for the driving cycle 2: (a) Fuel cell power trajectories, (b) Co-state trajectories, (c) State trajectories.

with the driving cycle. The mean amplitude of the gradient force can be more than other resistant forces except for the acceleration force, depending on driving cycles, as shown in Fig. 27. They are determined by using the longitudinal dynamic Eq. (1), and the mechanical braking is applied if the mechanical torque demand torque exceeds the maximal motor torque. As presented in Fig. 3, the driving cycle 2 owns the largest average value of the slope, while the driving cycle 3 the least value. This large gradient force results in a significant difference in the load power between uphills and downhills, and the estimate of the average fuel cell power is indirectly influenced. Therefore, the estimated average fuel cell power by using (25) is lower than the global average one, if the train first goes downhills and then go uphills, while the estimated average fuel cell power is higher than the global one reversely, which leads to a bad fuel economy of the strategies.

As the fuel cell power is eventually equal to the sum of various power loss due to energy conservation principle, the power demand to overcome slopes does not mean loss eventually, because the increased gravitational energy can be recycled in the future. Then the load power can be corrected by excluding the power to overcome the gradient slopes as follows:

$$P_{\text{load,cor}}(t) = P_{\text{load}}(t) - m\cdot g\cdot \sin\phi(t)\cdot v(t) + m\cdot g\cdot (\sin\overline{\phi})\cdot v(t), \tag{28}$$

then the estimate of the average fuel cell power can be improved

$$\overline{P}_{\text{fc},1}(t) = \frac{\int_0^t P_{\text{load,cor}}(\tau) + P_{\text{loss,bat}}(\tau)d\tau}{t}, \tag{29}$$

whereby the term $m\cdot g\cdot\sin\overline{\phi}$ represents the force required to overcome the average gradient, which corresponds to the height difference

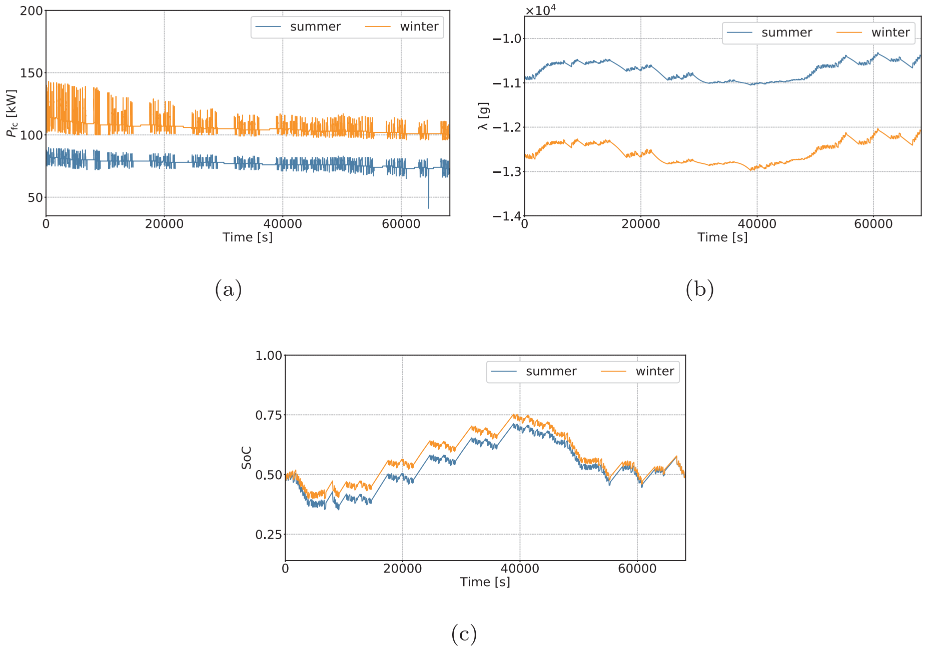

(a) (b)

(c)

Fig. 22. Results of PMP for the driving cycle 3: (a) Fuel cell power trajectories, (b) Co-state trajectories, (c) State trajectories.

Table 5
Results of offline PMP.

Cycles	$\overline{P}_{\text{load}}$ [kW]	$\overline{P}_{\text{loss,bat}}$ [kW]	$\overline{P}_{\text{fc}}$ [kW]	$\overline{\lambda}$ [g]	H_2 [kg/km]
1, summer	110.4	1.3	111.7	−12682	0.214
1, winter	139.2	1.3	140.5	−13301	0.280
2, summer	101.1	2.1	103.2	−12006	0.186
2, winter	129.8	2	131.9	−12771	0.296
3, summer	76.7	0.59	77.2	−10720	0.286
3, winter	105.3	0.56	105.9	−12551	0.421

between the start and end stations.

Another crucial point is linked to the long down time of regional trains in some stations, as presented in Fig. 3c for the driving cycle 3. The estimate of the average value by utilizing (29) can result in a significant increase of SoC during the long down time. In order to solve this problem, the down time and the travel time already experienced, and the total down time and travel time for each driving cycle, which are surely available in the area of railway transportation, are used to correct the estimate by weighting the corrected load power regarding driving and down time as follows:

$$\overline{P}_{\text{fc},2}(t)= \frac{1}{T}\cdot\frac{T_{\text{drive}}\cdot\int_{\text{driving}} P_{\text{load,cor}}(\tau)+P_{\text{loss,bat}}(\tau)\,d\tau}{T_{\text{driven}}}+ \frac{1}{T}\cdot\frac{T_{\text{stop}}\cdot\int_{\text{stopping}} P_{\text{load,cor}}(\tau)+P_{\text{loss,bat}}(\tau)\,d\tau}{T_{\text{stopped}}}, \qquad (30)$$

where T represents the total travel time, T_{stop} the total down time, T_{drive} the total driving time, T_{stopped} the experienced down time each time to update the average value, T_{driven} the experienced driving time. The sum of the corrected load power and the battery loss is integrated to calculate the energy consumption during driving and downtime separately. In this way, the estimate of the average value considers the future down time, and the over-charging of the battery system during the long down time can be avoided.

Furthermore, the difference between the integral of the sum of the corrected load power and the battery loss, and the supplied fuel cell power so far should be compensated in the future estimation of the average fuel cell power, to satisfy the charge-sustaining condition, as follows:

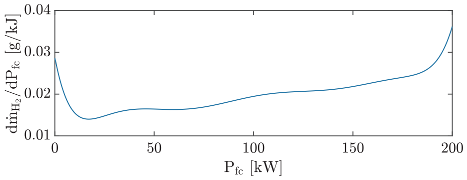

Fig. 24. Derivative of the mass flow with respect to the fuel cell power.

$$\overline{P}_{\text{fc,final}}(t) = \overline{P}_{\text{fc},2}(t) + \frac{\int_0^t (P_{\text{load,cor}}(\tau) + P_{\text{loss,bat}}(\tau) - P_{\text{fc}}(\tau))d\tau}{T - T_{\text{traveled}}}, \qquad (31)$$

where T_{traveled} represents the experienced travel time in each instant to update the average value.

If the SoC end target value is different from the initial value as in the case of a plug-in hybrid vehicle, an average power corresponding to the difference of battery energy should be added to that, and the average value can be reformulated as:

$$\overline{P}_{\text{fc,plug-in}}(t) = \overline{P}_{\text{fc,final}}(t) + \frac{\Delta E_{\text{bat}}}{T}, \qquad (32)$$

where ΔE_{bat} is the energy difference, which corresponds to the difference regarding the SoC values and T the total travel time.

4. Results

The simulation results by using the online APMP-based strategy are compared to the results of offline PMP with the load power trajectory and the SoC boundary values as the same as that under the APMP-based strategy. As the losses in R_1, R_2, and R_3 of the parallel branches of the battery system are not considered in implementating offline PMP, the fuel cell power from the results of offline PMP has to be corrected upwards by the sum of these losses. For that purpose, the battery current resulted from offline PMP flows through the three parallel R-C branches, as shown in Fig. 17. The corrected fuel cell power is then employed to calculate mass flow and total hydrogen consumption. It has to be mentioned that the corrected fuel cell power, in this way, is not wholly equivalent to optimal references. Nevertheless, it can be utilized to evaluate the APMP-based strategy without significant deviation. (see Fig. 28).

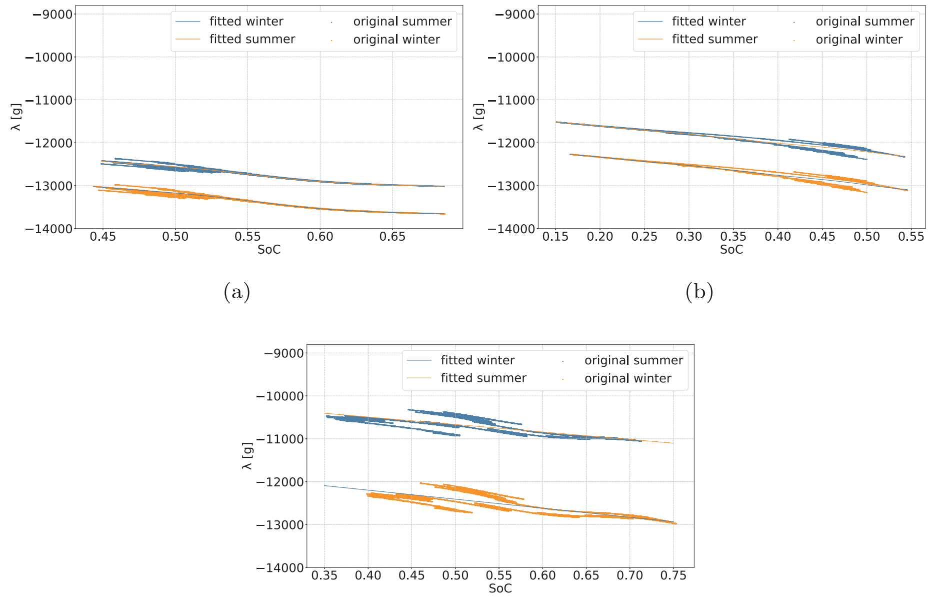

(a) (b)

(c)

Fig. 23. Dependency of the co-state on SoC under different weather conditions for different driving cycles: (a) Driving cycle 1, (b) Driving cycle 2, (c) Driving cycle 3.

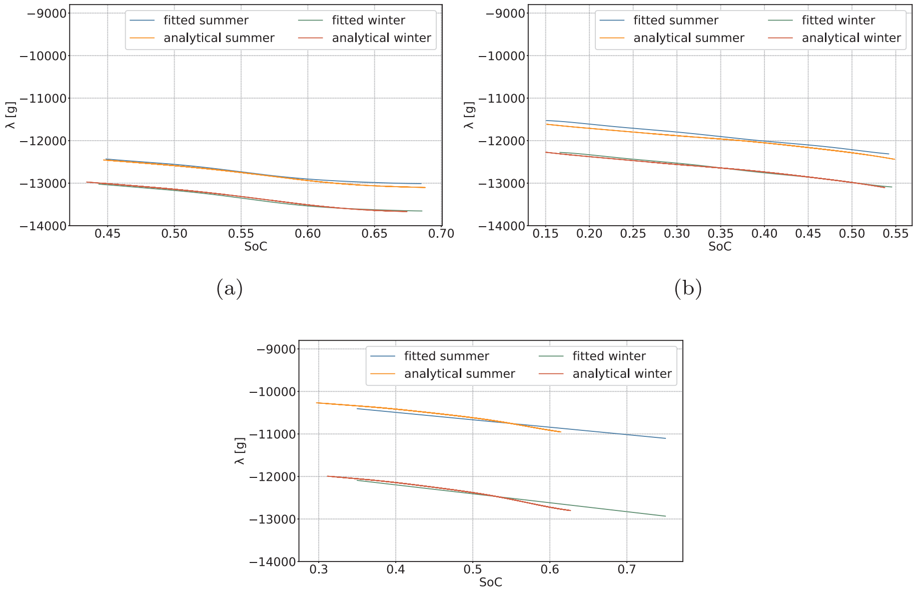

(a)

(b)

(c)

Fig. 25. Analytical determination of the co-state in function of SoC and the average fuel cell power for different driving cycles, compared to the fitted curve from offline results: (a) Driving cycle 1, (b) Driving cycle 2, (c) Driving cycle 3.

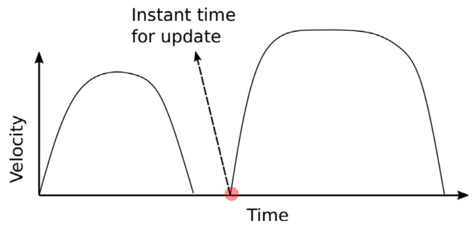

Fig. 26. schematic explaining the time instant to update the average fuel cell power.

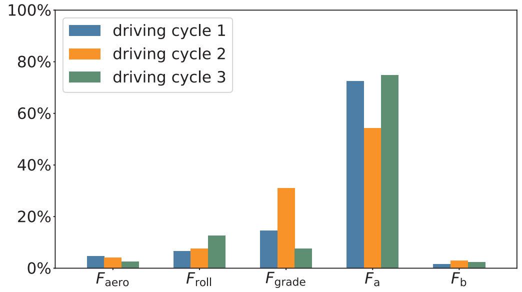

Fig. 27. Percentages of the average amplitude of different forces in total resistance force along the entire driving cycles.

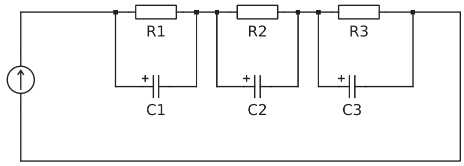

Fig. 28. Loss determination in parallel branches.

In the following parts, the trajectories from the APMP-based strategy for different driving cycles and weather conditions are displayed, together with that resulted from offline PMP. The initial SoC is 0.5 for all simulations.

Fig. 29 shows the fuel cell power trajectories for different driving cycles, including in summer and in winter, and they are compared to trajectories from offline PMP. The fuel cell system for all the three driving cycles works near the estimated average values with dynamic oscillation. Fast overlapping with the results of the offline PMP is observed under the driving cycle 3, while the fuel cell power trajectories are slight more different from the offline results of PMP under the other driving cycles, as shown in Fig. 29a and b. The reasons for that is that the estimated mean fuel cell power under driving cycle 2 and 3 are more deviated from the global average values, as shown in Fig. 30. Due to the shorter drive time of cycle 1 and 2 compared to the driving cycle 3, the deviation in the estimate of the average fuel cell power is obviously more. Although there are such deviations in the short-time scale, positive and negative deviations are compensated, which does not affect the fuel economy much. Therefore, an excellent fuel economy results, with more hydrogen consumption of 0.22%, 0.16%, 0.03% in summer, for driving cycle 1, driving cycle 2, driving cycle 3 respectively, compared to offline results, and more consumption of 0.24%, 0.22%, 0.03% in winter. The reason for that lies in the accurate estimates of the co-states along with the driving cycles.

Fig. 31 shows the co-state trajectories for different driving cycles, jointly with the co-state trajectories from offline PMP. The difference between APMP and offline PMP regarding the values of the co-state is small, with a maximal transient relative deviation of 5.2%, 5.5%, 4.3% in summer, for driving cycle 1, driving cycle 2, and driving cycle 3 respectively, and a maximal relative deviation of 6.8%, 8.3%, 1.2% in winter. Though a high deviation of the co-state happens at the beginning of the driving cycles, with the driving cycles running, the error in the estimates is reduced, which validates the robust adjustability of APMP. Besides that, It is obvious that the deviations in the case of the driving cycle 1 and 2 are more than that under the driving cycle 3. The reason lies in that the estimate of co-states is related to the average fuel cell power, which is more deviated from the global average values for the driving cycle 1 and 2. Regard the mean values of the co-states, they are summarized in Table 6, and a maximal deviations of 1.8% between APMP and offline PMP is observed.

Regarding the SoC trajectories shown in Fig. 32, They are fast overlapped with the results of offline PMP for all three driving cycles, which verifies the effectiveness of the APMP-based strategies. The SoC trajectories under different weather are fast the same. The reason lies in

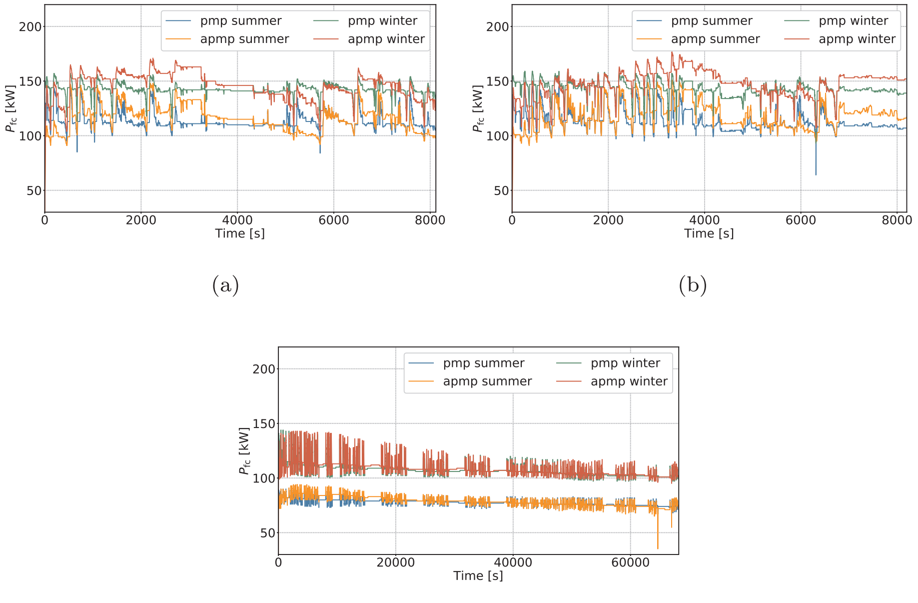

(a)

(b)

(c)

Fig. 29. Fuel cell power trajectories under APMP for different driving cycles, compared to that of PMP: (a) Driving cycle 1, (b) Driving cycle 2, (c) Driving cycle 3.

that under both weather conditions, the fuel cell system covers the average power, with about 30 kW more in winter than in summer due to the auxiliary consumption, and then the battery current under both conditions are fast the same. The end SoC values can be found in Table 6.

To test the effectiveness of this strategy in the long run, with components aging increased, the simulation is executed under an assumed battery capacity loss of 10% and a resistance increase of 5%. Here only the driving cycle 3 with the longest driving time is tested. The results are also compared to the results by using offline PMP strategy with the same aging degree considered. The state, co-state, and power trajectories are collected in Fig. 33, and a high overlapping is observed between APMP and PMP regarding the trajectories mentioned above. In terms of fuel economy, more hydrogen consumption of 0.11% and 0.08% compared to the results of offline PMP results for summer and winter, respectively, which means a slight increase of consumption when compared to the case without aging. In other words, the goodness of the fuel economy is maintained under the APMP-based strategy, and not much affected by the battery aging. The co-state is evaluated with a maximum relative deviation of 3.06% and 0.84% from the offline results, for summer and winter conditions, respectively. With the driving cycle continuing, the deviation decreases, as in the case of without aging considered. Therefore, the functionality of the APMP-based strategy is approved for the case of components aging.

It is worth mentioning that the depth of discharge under component is more than that without aging considered, as shown in Fig. 34b, which results from the decreased capacity of the battery system. In order to avoid over-charging and over-discharging of battery systems, information about the load in the future is required to adjust the estimate of the average fuel cell power, which belongs to future work. More notable is that the fuel cell power trajectories show more oscillations compared to that without aging, as shown in Fig. 34a, which results from increased resistance of the battery system. The reason behind that lies in that the strategy based on PMP tries to makes the fuel cell system work in the area of high efficiency on the one side and to reduces the battery loss on the other side, which is influenced by the strategy itself. When the battery resistance is low, it is more beneficial to maintain the fuel cell system to work close to the average values, and the battery loss is comparably small due to its small resistance. However, with the resistance increased due to the aging, the battery loss influences the fuel economy more, then the fuel cell system works with more oscillation. In this case, a weighting factor has to be introduced to balance the fuel economy and the stable operation of the fuel cell system.

5. Conclusions

A scalable, causal, adaptive optimal control-based energy management strategy for fuel cell hybrid trains is designed. As learned from the results of offline PMP, the convexity of the specific consumption curve is emphasized, which can be used to improve the fuel economy. More important is that the dependency of the co-state on SoC and the average fuel cell power is identified for the first time. With the help of reversely

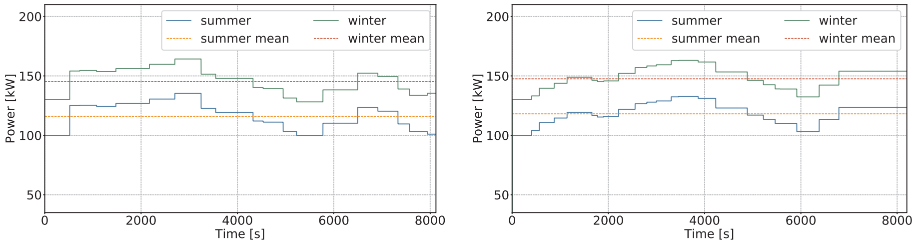

(a)

(b)

Fig. 30. Estimated Fuel cell power average trajectories under APMP for different driving cycles, compared to the global average values: (a) Driving cycle 1, (b) Driving cycle 2.

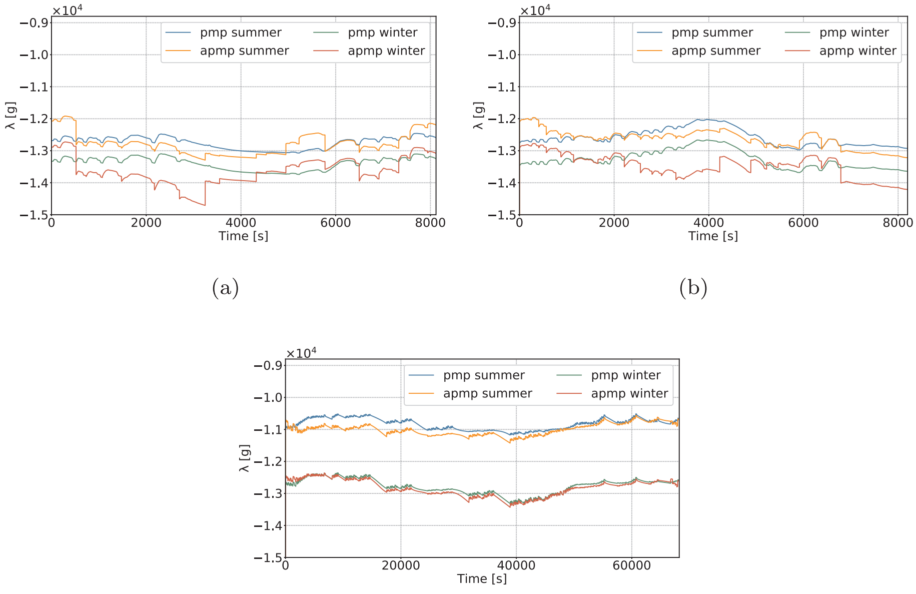

(a)

(b)

(c)

Fig. 31. Co-state trajectories under APMP for different driving cycles, compared to that of PMP: (a) Driving cycle 1, (b) Driving cycle 2, (c) Driving cycle 3.

Table 6
Simulation results of APMP.

Cycles	SoC_{end}	$\bar{\lambda}$ [g]	Ref. $\bar{\lambda}$ from PMP	H_2 [kg/km]	Ref. PMP
1, summer	0.5182	−12783	0.27%	0.223	0.22%
1, winter	0.5231	−13635	1.8%	0.291	0.24%
2, summer	0.6383	−12625	0.33%	0.218	0.16%
2, winter	0.6449	−13469	1.5%	0.284	0.22%
3, summer	0.5734	−10997	1.5%	0.303	0.03%
3, winter	0.623	−12833	0.45%	0.431	0.03%

using the optimal control theory, the dependency is analytically derived, which can be used to eliminate the sensitivity of APMP on the estimate of the co-state. Thereby, the co-state is corrected each time when the train leaves stations based on an estimated average fuel cell power, during the remaining time, the dynamic of the co-state is used to update the co-state. This average value is determined by using the history information, which ensures the strategy causality. Furthermore, the power demand due to gradient force is excluded in calculating the average power, which helps to reduce the oscillation of the estimate of the average value along with the variable gradient. Besides that, the total down time and the driving time accessible in railway transportation are used to improve the estimation of the average value, to avoid overcharging of batteries during the long down time. The accuracy of the estimated co-states, and the effectiveness of this strategy, under different weather, driving, and aging conditions, is validated by comparison to the results of offline PMP. Thereby a maximal deviation of 1.8% is observed in the co-state average value under different driving

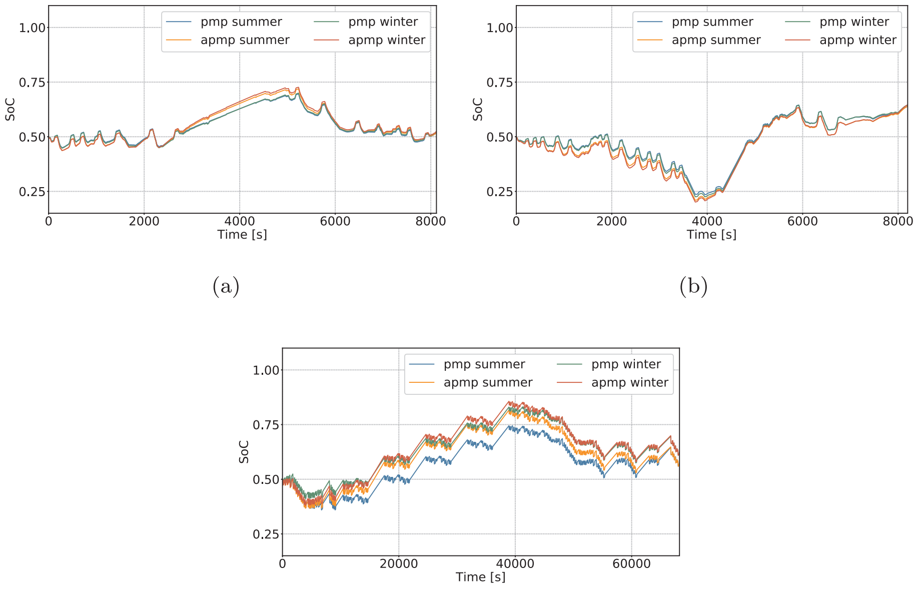

(a)

(b)

(c)

Fig. 32. State trajectories under APMP for different driving cycles, compared to that of PMP: (a) Driving cycle 1, (b) Driving cycle 2, (c) Driving cycle 3.

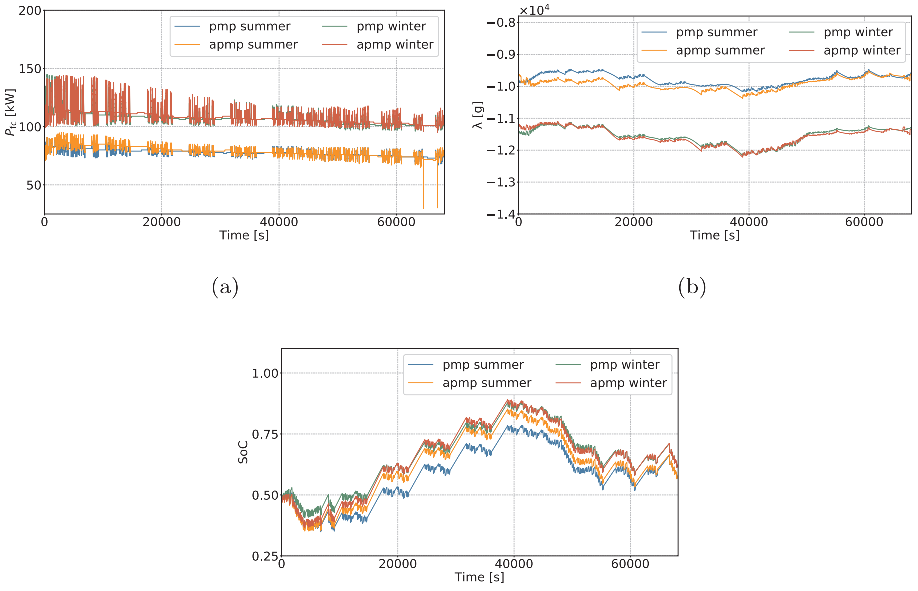

(a) (b)

(c)

Fig. 33. Results of APMP with aging considered, under the driving cycle 3, compared to corresponding offline results: (a) Fuel cell power trajectories, (b) Co-state trajectories, (c) State trajectories.

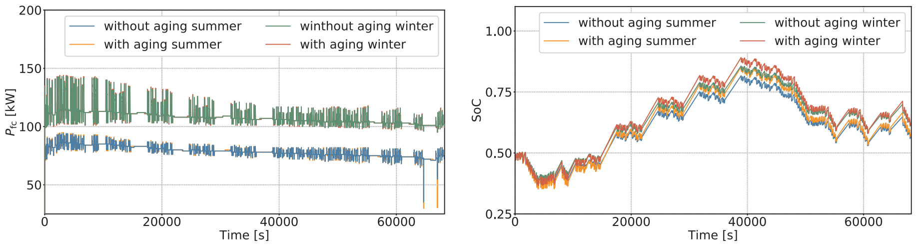

(a) (b)

Fig. 34. Comparison between the case with aging and the case without aging based on results of APMP for the driving cycle 3: (a) Fuel cell power trajectories, (b) State trajectories.

cycles in the case without aging. An excellent fuel economy under a typical driving cycle of regional railway transports in Berlin, with only 0.03% more consumption for both summer and winter conditions, when compared to the results of offline PMP, is resulted. Due to the model-based characteristics, the strategy can be scaled or transferred to other configuration systems or driving conditions without loss of effectiveness. In the future, the average fuel cell power can be more appropriately estimated by applying load information about upcoming routes, in order to avoid over-charging and over-discharging in the case of capacity loss of battery systems due to aging.

Declaration of Competing Interest

None.

References

[1] Percentage of the railway lines in use in europe in 2017 which were electrified, by country. <https://www.statista.com/statistics/451522/share-of-the-rail-network-which-is-electrified-in-europe/>, accessed November 30; 2019.

[2] Fernández-Dacosta C, Shen L, Schakel W, Ramirez A, Kramer GJ. Potential and challenges of low-carbon energy options: comparative assessment of alternative fuels for the transport sector. Appl Energy 2019;236:590–606.

[3] Miller AR, Peters J, Smith BE, Velev OA. Analysis of fuel cell hybrid locomotives. J Power Sources 2006;157(2):855–61.

[4] Development of the world's first fuel cell hybrid railcar. <https://www.jreast.co.jp/e/press/20060401/>, accessed December 18; 2019.

[5] Peng F, Chen W, Liu Z, Li Q, Dai C. System integration of china's first proton exchange membrane fuel cell locomotive. Int J Hydrogen Energy 2014;39(25):13886–93.

[6] Mugnetti P, Carbone S, Pede G. A fuelcell switcher locomotive with an hybridised propulsion system; 2006.

[7] Jürgen H. Auf dem Weg zur Null-Emmision, Eisenbahn-Magazin 2017;7:41.

[8] Brennstoffzellen: Siemens beauftragt ballard power. <https://www.iwr.de/news.php?id=34729>, accessed December 18; 2019.

[9] Fletcher T, Thring R, Watkinson M. An energy management strategy to concurrently optimise fuel consumption & pem fuel cell lifetime in a hybrid vehicle. Int J Hydrogen Energy 2016;41(46):21503–15.

[10] Tran D-D, Vafaeipour M, El Baghdadi M, Barrero R, van Mierlo J, Hegazy O. Thorough state-of-the-art analysis of electric and hybrid vehicle powertrains: topologies and integrated energy management strategies. Renew Sustain Energy Rev 2019;109596.

[11] Hofman T, Steinbuch M, Van Druten R, Serrarens A. Rule-based energy management strategies for hybrid vehicles. Int J Electric Hybrid Vehic 2007;1(1):71–94.

[12] Pielecha I, Cieślik W, Szałek A. The use of electric drive in urban driving conditions using a hydrogen powered vehicle-toyota mirai. Combust Eng 2018;57.

[13] Zhang P, Yan F, Du C. A comprehensive analysis of energy management strategies for hybrid electric vehicles based on bibliometrics. Renew Sustain Energy Rev 2015;48:88–104.

[14] Caux S, Hankache W, Fadel M, Hissel D. On-line fuzzy energy management for hybrid fuel cell systems. Int J Hydrogen Energy 2010;35(5):2134–43.

[15] Bellman R. The theory of dynamic programming. Bull Am Math Soc 1954;60(6):503–15.

[16] Peng H, Li J, Deng K, Thul A, Li W, Löwenstein L, et al., An efficient optimum energy management strategy using parallel dynamic programming for a hybrid train powered by fuel-cells and batteries. In: 2019 IEEE vehicle power and propulsion conference (VPPC); 2019. p. 1–7.

[17] Romaus C, Gathmann K, Böcker J. Optimal energy management for a hybrid energy storage system for electric vehicles based on stochastic dynamic programming. In:

2010 IEEE vehicle power and propulsion conference, IEEE; 2010. p. 1–6.

[18] Paganelli G, Guerra T, Delprat S, Guezennec Y, Rizzoni G. Optimal control theory applied to hybrid fuel cell powered vehicle. IFAC Proc Volumes 2002;35(1):253–8.

[19] Paganelli G, Delprat S, Guerra TM, Rimaux J, Santin JJ. Equivalent consumption minimization strategy for parallel hybrid powertrains. In: Vehicular technology conference. IEEE 55th Vehicular Technology Conference. VTC Spring 2002 (Cat. No. 02CH37367), Vol. 4, IEEE; 2002. p. 2076–81.

[20] Park J, Park J-H. Development of equivalent fuel consumption minimization strategy for hybrid electric vehicles. Int J Autom Technol 2012;13(5):835–43.

[21] Lei Z, Qin D, Hou L, Peng J, Liu Y, Chen Z. An adaptive equivalent consumption minimization strategy for plug-in hybrid electric vehicles based on traffic information. Energy 2019;116409.

[22] Sciarretta A, Back M, Guzzella L. Optimal control of parallel hybrid electric vehicles. IEEE Trans Control Syst Technol 2004;12(3):352–63.

[23] Zhang C, Vahid A. Real-time optimal control of plug-in hybrid vehicles with trip preview. Proceedings of the 2010 American Control Conference, IEEE. 2010. p. 6917–22.

[24] Rezaei A, Burl JB, Solouk A, Zhou B, Rezaei M, Shahbakhti M. Catch energy saving opportunity (ceso), an instantaneous optimal energy management strategy for series hybrid electric vehicles. Appl Energy 2017;208:655–65.

[25] Onori S, Tribioli L. Adaptive pontryagin's minimum principle supervisory controller design for the plug-in hybrid gm chevrolet volt. Appl Energy 2015;147:224–34.

[26] Serrao L, Onori S, Rizzoni G. A comparative analysis of energy management strategies for hybrid electric vehicles. Proc Inst Mech Eng, Part D: J Autom Eng 2011;133 (3): 60.

[27] Xie S, Hu X, Xin Z, Brighton J. Pontryagin's minimum principle based model predictive control of energy management for a plug-in hybrid electric bus. Appl Energy 2019;236:893–905.

[28] Ali AM, Söffker D. Towards optimal power management of hybrid electric vehicles in real-time: a review on methods, challenges, and state-of-the-art solutions. Energies 2018;11(3):476.

[29] Miyatake M, Ko H. Optimization of train speed profile for minimum energy consumption. IEEJ Trans Electr Electron Eng 2010;5(3):263–9.

[30] Migliardini F, Veneri O, Corbo P. Hydrogen and proton exchange membrane fuel cells for clean road transportation. J Industr Eng Chem 2011;17(3):633–41.